

Double-Edge Detection of Radiographic Lumbar Vertebrae Images Using Pressurized Open DGVF Snakes

Sridharan Kamalakannan*, Arunkumar Gururajan, *Member, IEEE*, Hamed Sari-Sarraf, Rodney Long, *Member, IEEE*, and Sameer Antani

Abstract—The detection of double edges in X-ray images of lumbar vertebrae is of prime importance in the assessment of vertebral injury or collapse that may be caused by osteoporosis and other spine pathology. In addition, if the above double-edge detection process is conducted within an automatic framework, it would not only facilitate inexpensive and fast means of obtaining objective morphometric measurements on the spine, but also remove the human subjectivity involved in the morphometric analysis. This paper proposes a novel force-formulation scheme, termed as pressurized open directional gradient vector flow snakes, to discriminate and detect the superior and inferior double edges present in the radiographic images of the lumbar vertebrae. As part of the validation process, this algorithm is applied to a set of 100 lumbar images and the detection results are quantified using analyst-generated ground truth. The promising nature of the detection results bears testimony to the efficacy of the proposed approach.

Index Terms—Directional gradient vector flow (DGVF) snakes, double edges, energy minimization, lumbar vertebrae, pressure force.

I. INTRODUCTION

THE LOWER back (lumbar) region of the human spinal column is composed of a set of five vertebrae, commonly referred to as L1 through L5 [see Fig. 1(a)]. These vertebrae carry the maximal percent of the body weight and are usually subject to the largest forces and stresses along the spine [1]. Pathology on these vertebrae can be associated with backpain-related ailments. Therefore, early diagnosis/detection of these spinal disorders is of great interest to the osteoarthritis research community.

The Lister Hill National Center for Biomedical Communications, an R&D division of the National Library of Medicine (NLM), has archived a large repository of around 8000

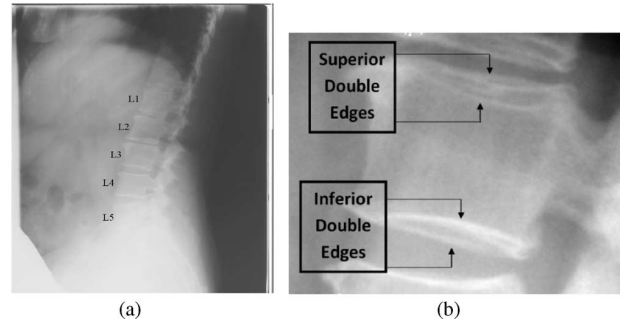


Fig. 1. (a) L1-L5 marked in a radiographic lumbar image. (b) Superior and inferior double edges.

radiographic lumbar images, in collaboration with the National Center for Health Statistics and the National Institute of Arthritis and Musculoskeletal and Skin Diseases. Researchers at NLM aim to classify vertebrae from the collected images as normal or abnormal for conditions of interest to the osteoarthritis community. For similar reasons, a number of researchers in the computer vision community have developed methods for extracting morphometric measurements from the radiographic lumbar vertebrae images [2]–[6].

In order to elicit the aforementioned morphometric measurements, one needs to accurately extract a corresponding set of vertebral morphometric points by segmenting the upper and lower end plates of each of the five lumbar vertebrae. However, in radiographic lumbar images, these vertebral end plates mostly occur as double edges [see Fig. 1(b)] due to a combination of some or all of the following factors: 1) an oblique viewing angle of the vertebra relative to the X-ray beam; 2) the projective nature of the X-ray image, which shows edges that would normally be hidden by the vertebral body; and 3) differential edge height between the near and far edges, which may be due to anatomy, injury, and/or pathology. This double-edge phenomenon on lateral radiographs is well-known in the radiographic community and has been discussed and illustrated in the published literature [7].

As prescribed in [2] and [7], various vertebral morphometric measurements can be made by accurately identifying six morphometric points that are as shown in Fig. 2. In this illustration, one can notice that the middle superior and the middle inferior morphometric points are marked midway between the two double edges that represent the superior and the inferior end plates, respectively. Hence, this method of morphometric

Manuscript received March 10, 2009; revised June 30, 2009, August 21, 2009 and November 1, 2009; accepted December 4, 2009. Date of publication February 17, 2010; date of current version May 14, 2010. This work was supported in part by the Intramural Research Program of the National Institutes of Health, in part by National Library of Medicine, and in part by the Lister Hill National Center for Biomedical Communications. Asterisk indicates corresponding author.

*S. Kamalakannan is with the Texas Tech University, Lubbock, TX 79415 USA (e-mail: sridharan.kamalakannan@ttu.edu).

A. Gururajan and H. Sari-Sarraf are with the Texas Tech University, Lubbock, TX 79415 USA (e-mail: arunkumar.gururajan@ttu.edu; hamed.sari-sarraf@ttu.edu).

R. Long and S. Antani are with the National Institutes of Health, Bethesda, MD 20892 USA (e-mail: rlong@mail.nih.gov; santani@mail.nih.gov).

Color versions of one or more of the figures in this paper are available online at <http://ieeexplore.ieee.org>.

Digital Object Identifier 10.1109/TBME.2010.2040082

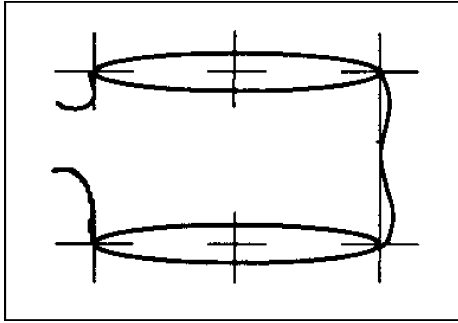


Fig. 2. Illustrating the six morphometric points that are generally used to make various morphometric measurements [2].

point placement clearly requires the detection of the said double edges, which is performed either implicitly [2], [8] or explicitly [7], [9] by radiologists during the process of assessing spine pathology [10].

In the past, others [3]–[6], [11]–[15] have proposed various segmentation methods to delineate the lumbar vertebrae in the spine radiographs. The research conducted in [3] and [4] elaborates on an automatic delineation technique, wherein the authors use an edge detection scheme coupled with *a priori* knowledge to identify the edges corresponding to the lumbar vertebrae. The work performed by Casciaro and Massotier [5], automatically segments the lumbar vertebrae by first enhancing the vertebral edges in the frequency domain and subsequently employing a shape recognition function to identify potential vertebral borders. Cherukuri *et al.* [6], present a semiautomatic segmentation technique, wherein radiologists mark 7–9 points along the vertebra's body. To generate a closed boundary, the expert-generated points are connected together by employing a second-order B-spline algorithm. The works detailed in [11]–[15] adopt a shape-based segmentation approach using deformable models to automatically delineate the vertebral boundaries. In particular, the research in [11] and [12] utilizes active shape models (ASM), whereas those in [13] and [14] utilize active appearance models (AAM) for segmenting the lumbar vertebrae. The work conducted in [15] adopts a hierarchical shape-based approach to segmenting the lumbar vertebrae, wherein the generalized hough transform (GHT) is employed to initialize AAM. However, the aforementioned methods, while reasonably successful in segmenting the vertebral body, do not address one significant aspect of lumbar vertebrae segmentation. Specifically, they stop short of detecting the double edges of each vertebra. Research results for double-edge detection in the published literature appear to be quite rare. Gardner *et al.* [9] has extensively discussed the measurement errors resulting from neglecting the double edges, and further, demonstrated double-edge detection using an active contour approach. The snake model in [9], however, is initialized using operator-provided points and also the procedure has not been validated on a sizeable dataset of images.

In this paper, we propose a novel force-formulation algorithm, referred to as pressurized open directional gradient vector flow (PODGVF) that automatically and accurately detects the double edges in the lumbar vertebrae. In particular, this approach uses a set of four open-contour snakes, wherein a pressure force term

is combined with the recently introduced directional gradient vector flow (DGVF) snakes [16], [17] to differentiate and detect the superior and inferior double edges. The pressure forces in the deformable model are constructed to overcome the noise in the image and also to reduce the influence of the neighboring vertebra on the double-edge detection result. It is noteworthy that PODGVF can readily handle vertebrae that appear to have single superior and inferior edges. This is an important feature of the proposed method, as the presence of double edges is not always guaranteed. The approach has been validated on a set of 100 lumbar spine radiographs. In each of these cases, the detection results have been computed and quantified using analyst-generated, radiologist-verified ground truth. These results look promising for extending the automated analysis of spine pathologies with capability to handle double edges.

This paper is organized as follows. Section II explains the algorithm used for detecting the double edges, starting with an overview of parametric snakes and further explaining the formulation of the force equations that constitute the PODGVF snakes. Finally, this section discusses the step-by-step approach used to detect the double edges. Section III discusses the experimental results of the double-edge detection scheme on a set of 100 spine radiographs, and illustrates the role of the detected double edges in computing morphometric features for characterizing vertebral deformities in the lumbar spine. Finally, the last section presents the conclusions of this paper.

II. TECHNICAL APPROACH: PODGVF SNAKES

We give a brief overview of parametric snakes before discussing the algorithm. A snake contour is represented parametrically as $V(s) = [x(s), y(s)]$, where “ s ” is the arc length normalized from 0 to 1 (in the continuous case). In discrete terms, snakes essentially consist of a set of control points, connected by straight lines. The properties of a snake can be formulated through an energy function. Based on prior knowledge of the application, the energy function could be appropriately specified by the user. On every iteration, the snake contour evolves such that it leads to reduction in its energy. Typically, the energy function for a snake can be subdivided into internal and external energies. Thus, the total energy is given by

$$E_{\text{snake}} = \int_{s=0}^1 (E_{\text{internal}}(V(s)) + E_{\text{external}}(V(s))) ds \quad (1)$$

where E_{snake} , E_{internal} , and E_{external} represent the total, internal, and external energies of the snake, respectively.

Internal energy depends on the properties of the contour, such as length, curvature, and area enclosed, whereas external energy depends on the image features such as edges. As mentioned earlier, the goal is to derive a force that minimizes the total energy of the snake. This can be done by using the calculus of variations method [18]. This derived force is responsible for driving the contour to the desired location. This force can be expressed as follows:

$$F_x = F_{x,\text{internal}} + F_{x,\text{external}} \quad (2)$$

$$F_y = F_{y,\text{internal}} + F_{y,\text{external}} \quad (3)$$

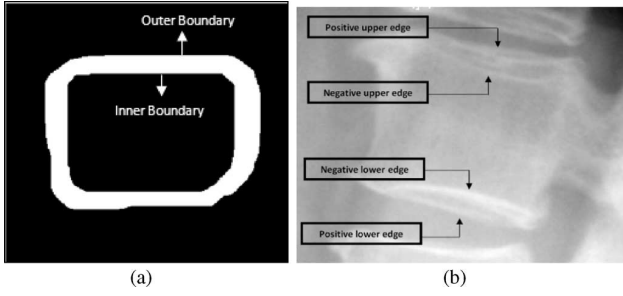


Fig. 3. (a) Illustration of the concept of a positive and negative edge. (b) Labeling of double edges present in the lumbar vertebra.

where F_x and F_y are the overall forces that drive the contour in the x - and y -directions, respectively. $F_{x,\text{internal}}$ and $F_{y,\text{internal}}$ are the internal forces, whereas $F_{x,\text{external}}$ and $F_{y,\text{external}}$ are the external forces in the x - and y -directions, respectively.

The following section explains the formulation of the force equations in the context of the current application.

A. Formulating Force Equations to Detect Double Edges

Before setting up the force equations for this application, it is essential to establish the concept of a positive and a negative edge. In a gray level image, a positive edge or a negative edge occurs when the intensity gradients along a boundary point inward or outward, respectively. For illustrative purposes, consider Fig. 3(a), which shows a rectangular object with an inner and outer boundary. The positive edge is taken to be the outer boundary and the negative edge is considered to be the inner boundary. Hence, in the current application, the outer boundaries of the double edges are labeled as positive upper and lower edges, whereas the inner boundaries of the double edges are labeled as negative upper and lower edges [see Fig. 3(b)]. Four snakes with open contours are used to detect these four edges independently. All these snakes are driven by a customized combination of internal and external forces that minimize the energy of the snakes at every iteration.

1) *Internal Force Formulation:* The internal energy functional of the four snakes are given by

$$E_{\text{internal}} = \int_{s=0}^1 \left(\alpha \left| \frac{dV(s)}{ds} \right|^2 + \beta \left| \frac{d^2V(s)}{ds^2} \right|^2 - \rho \int A \right) ds. \quad (4)$$

The first term $\alpha |dv(s)/ds|^2$ is generally referred to as the elastic energy (E_{elastic}). Here, E_{elastic} is proportional to the length of the contour and α is the weight parameter associated with the elastic energy term. The second term $\beta |d^2V(s)/ds^2|^2$ is generally referred to as the bending energy (E_{bending}). Here, E_{bending} depends on the curvature of the contour and β is the weight parameter associated with the bending energy term. α and β are positive constants. Minimization of the first two terms in the internal energy equation will make the snake smooth and continuous. These two terms are similar to the internal energies used in Kass snakes [19]. The last term $-\rho \int A$ is called the pressure energy (E_{pressure}) and is directly proportional to the negative of the area of the contour. Here, A is the area enclosed

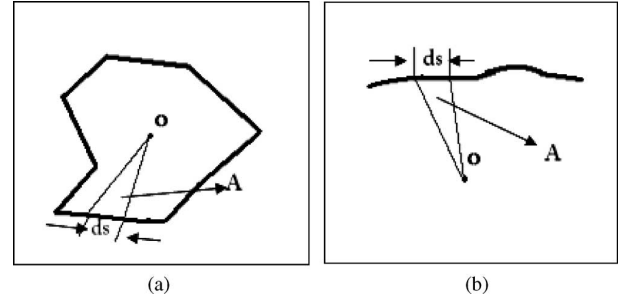


Fig. 4. (a) Area (A) enclosed by an elemental length ds and the origin (O) in case of a closed contour. (b) Area (A) enclosed by an elemental length ds and an arbitrary origin (O) just below the open contour.

by an elemental length ds and the origin of the contour [see Fig. 4(a)] and ρ is a constant. In the context of the current application, where open contours are used, A is defined with respect to the image origin, which remains below the open contour as shown in Fig. 4(b). Depending on whether ρ is positive or negative, the contour expands (moves up in case of an open contour) or contracts (moves down in case of an open contour), respectively. In this particular application, ρ is chosen to be positive or negative depending on the edge that is being detected. The procedure used to determine the sign of ρ is discussed next.

Minimizing the internal energy using calculus of variations will give rise to internal forces that drive the contour. This can be expressed as follows:

$$F_{x,\text{internal}} = -\alpha \frac{d^2x(s)}{ds^2} + \beta \frac{d^4x(s)}{ds^4} + \rho \frac{dy(s)}{ds} \quad (5)$$

$$F_{y,\text{internal}} = -\alpha \frac{d^2y(s)}{ds^2} + \beta \frac{d^4y(s)}{ds^4} - \rho \frac{dx(s)}{ds}. \quad (6)$$

Here, $F_{x,\text{internal}}$ and $F_{y,\text{internal}}$ represent the internal forces acting on the point $(x(s), y(s))$ in the x - and y -directions, respectively. Each of the four snakes used to detect the double edges are assigned to the same elastic and bending forces, i.e., they have the same α and β values. However, the sign of ρ used for the snakes responsible for detecting the positive upper edge and the negative lower edge is positive, giving rise to a *compressive* pressure force, whereas the sign of ρ used for the snakes responsible for detecting the positive lower edge and the negative upper edge is negative, giving rise to an *expansive* pressure force. There are two main reasons for selecting appropriate pressure forces for these four open snakes: 1) to avoid the snakes getting “stuck” in regions of local noise; and 2) to reduce the influence of the neighboring vertebrae. The following two paragraphs will explain these reasons in detail.

First, we discuss the effect of noise on the snake evolution. The preprocessed image (see Section II-B3) has local high gradients (noise) that can be simulated by using any noise model that approximates the spike like salt and pepper noise. Fig. 5 shows a synthetic model of the lumbar vertebra with double edges, corrupted with salt and pepper noise. Consider an arbitrary initialization [shown in red in Fig. 6(a)] of a snake intended to detect the positive upper edge. The internal forces used to drive this snake are the elastic and bending forces. Note that for this

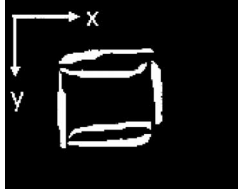


Fig. 5. Synthetic model of a lumbar vertebra with double edges corrupted with salt and pepper noise.

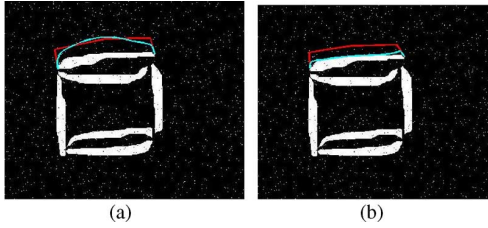


Fig. 6. Initialization is shown in red and the final result in cyan. (a) Final contour gets latched on to the local image noise. (b) Final contour overcomes local image noise and gets latched on to the positive upper edge due to the compression pressure force.

snake, no pressure force is used. The external forces are constructed so that the contour is driven to places of high gradients in the image. The result after 300 iterations is shown in cyan in Fig. 6(a). We notice that the snake has “latched on” to the local noise. Now consider the snake initialized in red in Fig. 6(b). In addition to all the forces used for the snake in Fig. 6(a), this snake [in Fig. 6(b)] is also driven by additional compressive pressure force. The result after 300 iterations is shown in cyan. We observe that the compressive pressure force pushes the snake downward and overcomes the influence of the local noise. This suggests that appropriate selection of the sign of ρ for the four open contours will mitigate the effect of local noise on the final detection result.

Another reason for using the pressure force is to reduce the influence of neighboring vertebrae on the detection result. Consider Fig. 7(a), which shows a part of the neighboring vertebrae. An arbitrary initialization to detect the positive upper edge is shown in red, and the final result (using all except pressure forces) after 300 iterations is shown in cyan. One can notice that the initialization is close to a neighboring vertebra, which results in an incorrect result. Now consider Fig. 7(b) that shows the result in cyan with a similar initialization as in Fig. 7(a) (in red), but with an additional compression pressure force. We observe that the usage of appropriate pressure forces appears to reduce or eliminate the influence of the neighboring vertebrae. This concludes the description of the formulation of internal energies and their corresponding forces for this application. The next section will concentrate on the formulation of external forces.

2) *External Force Formulation:* The snake initializations shown in Figs. 6 and 7 were located completely above the positive upper edge. Now, consider the snake initialization (red) and the corresponding result (cyan) obtained by using the balloons [20], shown in Fig. 8(a). The balloon snake is only partially able to detect the positive upper edge, as it cannot discriminate between an inner and outer edge. In order to avoid this problem,

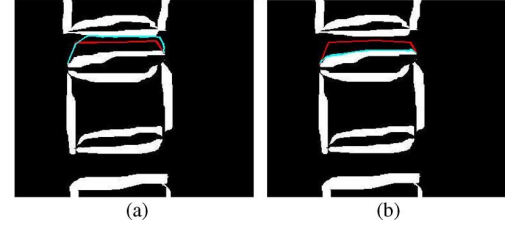


Fig. 7. Initialization is shown in red and the final result in cyan. (a) Final contour gets latched on to the neighboring vertebra. (b) Final contour eliminates the influence of the neighboring vertebra and gets latched on to the positive upper edge.

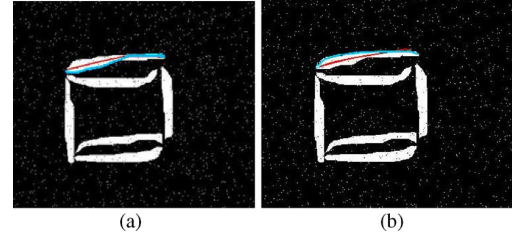


Fig. 8. Initialization is shown in red and the final result in cyan. (a) Balloons do not have the ability to distinguish between an inner and outer boundary. (b) DGVF snakes are able to accurately discriminate between an inner and outer boundary.

the DGVF [16] snakes are used, which are designed to discriminate an inner and outer edge. Fig. 8(b) shows an implementation of a DGVF snake with a similar initialization as in Fig. 8(a). We note that the DGVF snake completely detects the positive upper edge, while ignoring the negative upper edge. This is the main motivation for selecting the external forces, employed in DGVF snakes, for this application.

The external force that drives these snakes is posed as a force balance condition instead of a typical energy minimization problem. Two different types of external DGVF forces are formulated to detect the four double edges: 1) a positive DGVF force to detect the positive upper and lower edges and 2) a negative DGVF force to detect the negative upper and lower edges. The mathematical framework for these forces is illustrated as follows.

Consider the synthetic image of a lumbar vertebra shown in Fig. 9(a). Let g be the gradient of this image. For positive edges, one can define as follows:

$$f_x^+(x, y) = \max \{g_x(x, y), 0\} \quad (7)$$

$$f_x^-(x, y) = -\min \{g_x(x, y), 0\} \quad (8)$$

$$f_y^+(x, y) = \max \{g_y(x, y), 0\} \quad (9)$$

$$f_y^-(x, y) = -\min \{g_y(x, y), 0\} \quad (10)$$

and similarly, for the negative edges

$$f_x^+(x, y) = -\min \{g_x(x, y), 0\} \quad (11)$$

$$f_x^-(x, y) = \max \{g_x(x, y), 0\} \quad (12)$$

$$f_y^+(x, y) = -\min \{g_y(x, y), 0\} \quad (13)$$

$$f_y^-(x, y) = \max \{g_y(x, y), 0\} \quad (14)$$

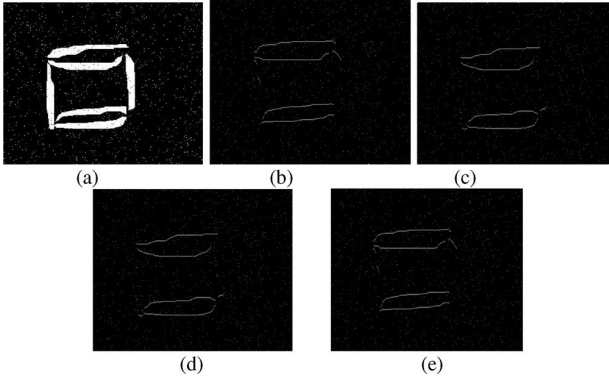


Fig. 9. (a) Synthetic lumbar image. (b) f_y^+ for positive edges. (c) f_y^- for positive edges. (d) f_y^+ for negative edges. (e) f_y^- for negative edges.

Here, g_x and g_y are the partials of g with respect to x and y , respectively. For positive edges, f_x^+ , f_x^- , f_y^+ , and f_y^- represent the gradient of the positive edges in x -, $-x$ -, y -, and $-y$ -directions, respectively. Fig. 9(b) and (c) shows f_y^+ and f_y^- as calculated by using (9) and (10), respectively. For negative edges, f_x^+ , f_x^- , f_y^+ , and f_y^- represent the gradient of the negative edges in x -, $-x$ -, y -, and $-y$ -directions, respectively. Fig. 9(d) and (e) shows f_y^+ and f_y^- as calculated by using (13) and (14), respectively.

Within this setup, one can define the DGVF field as a 4-D vector field represented by

$$D(x, y) = [u^+(x, y), u^-(x, y), v^+(x, y), v^-(x, y)] \quad (15)$$

where u^+ , u^- , v^+ , and v^- are obtained by solving the four equations as follows:

$$\mu \nabla^2 u^+ - (u^+ - df_x^+)(df_x^+)^2 = 0 \quad (16)$$

$$\mu \nabla^2 u^- - (u^- - df_x^-)(df_x^-)^2 = 0 \quad (17)$$

$$\mu \nabla^2 v^+ - (v^+ - df_y^+)(df_y^+)^2 = 0 \quad (18)$$

$$\mu \nabla^2 v^- - (v^- - df_y^-)(df_y^-)^2 = 0. \quad (19)$$

In the aforementioned set of equations, μ is a positive constant. It is important to have a physical interpretation of the aforementioned set of four equations, since they play an important part in the evolution of the DGVF snakes. Accordingly, these equations are interpreted next by considering (16) as an example.

- 1) If $|df_x^+|^2$ is small (which happens in the smooth or uniform regions of the image), (16) will be dominated by the first term, and therefore, approximated as follows:

$$\mu \nabla^2 u^+ = 0. \quad (20)$$

Solving this diffusion equation with initial condition $u_0^+ = f_x^+$, results in a smooth interpolation of f_x^+ from the boundary. Applying the same logic to all the four equations, the components of the DGVF field will be a smoothly varying field in the uniform regions of the image.

- 2) If $|df_x^+|^2$ is large (which happens near the edges), (16) will be dominated by the second term and can be approximated

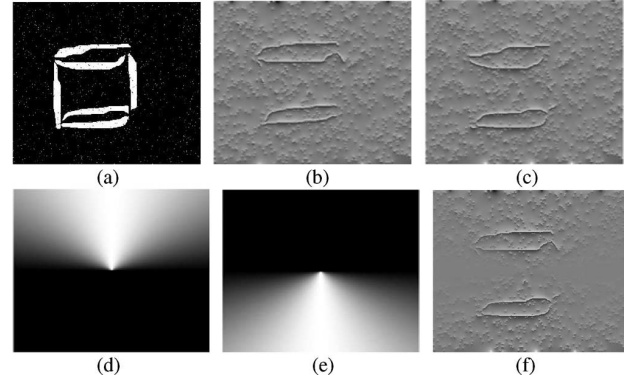


Fig. 10. (a) Synthetic lumbar image. (b) v^+ for positive edges. (c) v^- for positive edges. (d) $\max\{\sin(\theta), 0\}$. (e) $-\min\{\sin(\theta), 0\}$. (f) $F_{y,\text{external}}$ for positive edges.

as follows:

$$(u^+ - df_x^+)(df_x^+)^2 = 0. \quad (21)$$

Solving this equation results in $u^+ = df_x^+$ at the edges. Again, applying the same logic to the remaining equations (17)–(19), one can see that the components of the DGVF field have a high value near the appropriate edges.

Next, if one considers θ to be the contour's normal direction at a particular "snaxel" (snake's control point or element), then the external DGVF forces in the x - and y -directions are given by

$$F_{x,\text{external}} = u^+ \times \max\{\cos(\theta), 0\} - u^- \times -\min\{\cos(\theta), 0\} \quad (22)$$

$$F_{y,\text{external}} = v^+ \times \max\{\sin(\theta), 0\} - v^- \times \min\{\sin(\theta), 0\}. \quad (23)$$

Depending on the manner in which the fields are constructed, the external forces [calculated from (22) and (23)] will be accordingly used to detect either the positive or the negative edges. A pictorial illustration of (23) is shown in Fig. 10, for the case of fields set up to detect the positive edges. Fig. 10(b) and (c) shows the fields corresponding to v^+ and v^- , respectively. Fig. 10(d) and (e) shows a visual representation of $\max\{\sin(\theta), 0\}$ and $-\min\{\sin(\theta), 0\}$, respectively. Fig. 10(f) shows the external force field in the y -direction (23). We observe from Fig. 10(f) that $F_{y,\text{external}}$ consists only of the edges corresponding to the y component of the positive edges. In Fig. 10(f), note that all the negative edges are eliminated, since the DGVF fields have been constructed to detect the positive edges, thus giving the snake the ability to distinguish between a positive and a negative edge.

To conclude, among the four snakes used, two employ positive DGVF forces and the other two employ negative DGVF forces as their external forces. Since all the four snakes are open contoured and use additional pressure forces, we term them PODGVF snakes. In the Section II-B, we explain in detail, the step-by-step procedure followed to detect these double edges.

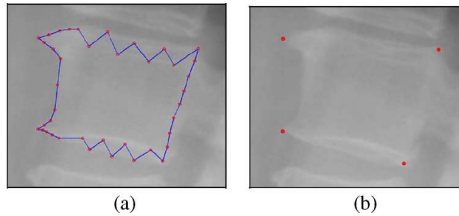


Fig. 11. (a) ASM result of a single lumbar vertebra. (b) Four detected corner points.

B. Customizing PODGVF Snakes to Detect Vertebral Double Edges

In the following sections, we describe the sequence of steps used in tailoring the PODGVF snakes to detect the vertebral double edges.

1) *Detecting Vertebra Corners*: The first step in the detection of double edges lies in estimating the locations of the vertebra corners, which in turn, can be obtained by segmenting the radiographic lumbar vertebrae. Therefore, before delving into the corner detection step, it would be appropriate to provide a brief overview of the past research that has been conducted by the authors with regard to lumbar vertebrae segmentation.

A hierarchical three-step procedure, consisting of: 1) coarse segmentation; 2) fine segmentation; and 3) double-edge detection, has been adopted to segment the radiographs. The details of the work conducted with regard to coarse and fine segmentation can be found in [11] and [15]. The coarse segmentation of the lumbar vertebra is performed using a customized version of the GHT [15] that provides for a robust approximation of the pose of the vertebrae, which in turn, is used as initialization to the fine segmentation stage, wherein a customized ASM is employed to provide the final segmentation. Finally, it is worth mentioning that after conducting an extensive study involving 2000 lumbar spine radiographs, it was observed that the output of the first two steps of our approach provided an acceptable segmentation result in around 80% of the cases. In these 80% cases, the result provided by ASM is used to facilitate the placement of the corner points for the purpose of double-edge detection.

Consider the lumbar vertebra and its corresponding ASM segmentation (red points) shown in Fig. 11(a). We use the ASM result, obtained by using the procedure outlined in [11], for snake initialization and for establishing a region of interest. The ASM result is first employed to find the four corners of the vertebra, as described next.

We adopt the following sequence of steps to find the vertebra corners from the ASM result.

- 1) The distance and the slope between every pair of points on the segmented ASM boundary are calculated.
- 2) Each pair of points is separated into one of two categories, depending on whether the slope is positive or negative. The points corresponding to zero or infinity slopes are special cases, and are arbitrarily placed in either of the two categories.
- 3) The pairs of points corresponding to the maximum distances in each category are selected as the vertebra corners. These four points are shown in Fig. 11(b).

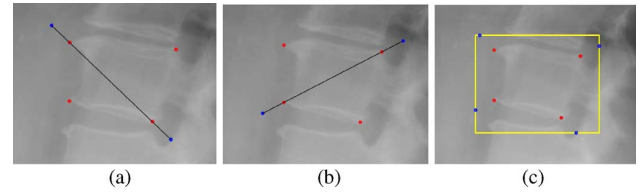


Fig. 12. (a) and (b) Determining the outer diagonal points to establish a region of interest. (c) Region of interest for a single lumbar vertebra.

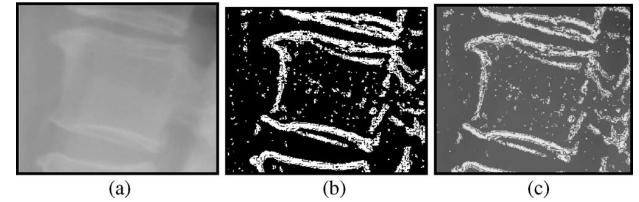


Fig. 13. (a) Gray level image of a lumbar vertebra. (b) Edge image. (c) Blended image.

This procedure is repeated for all five vertebrae.

2) *Establishing Region of Interest*: A region of interest is then established for each of the five lumbar vertebrae using the identified corner points. This is done to reduce the computational cost that would otherwise be required to compute the DGVF field for the entire image. The region of interest is selected as follows.

- 1) For each of the two diagonals, the corner points on the diagonal are selected, and two points (blue color) are marked at an empirically selected distance of 40 pixels (so that the points always lie well outside the vertebra) on either side of the selected points as shown in Fig. 12(a) and (b).
- 2) A region of interest is constructed using these four points as shown in Fig. 12(c). All ensuing calculations for each vertebra are done within the established regions of interest.
- 3) *Preprocessing for Noise Removal and Edge Enhancement*: The main objectives in the preprocessing step [11] are the enhancement of the image and elimination of noise while preserving the double edges. As a first step, the image is high-pass filtered, i.e., the edges are enhanced using unsharp masking, followed by thresholding. For this purpose, a Gaussian mask of size $N \times N$ and standard deviation σ is used for blurring the image; subtraction of the blurred from the original results in edge enhancement; this is followed by Otsu's thresholding [21], which binarizes the image. These edge images are extracted for five different values of N and σ , and are subsequently combined using an EXCLUSIVE OR operation. To preserve the double edges, which might be lost during edge extraction (due to poor contrast), the original gray level image is combined with its corresponding edge image. This procedure is termed as blending [11], and is produced by taking the average of the original gray level image with the edge image, as shown in Fig. 13.
- 4) *Initialization of Open Contours*: Four open contours are initialized for the four boundaries discussed in the previous step. The control points for these contours are selected as follows.
 - 1) The midpoints of the upper and lower corner points are determined, as shown in Fig. 14(a).

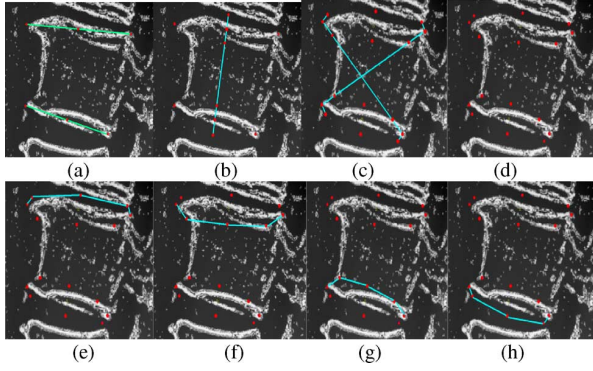


Fig. 14. Initialization of four open snake contours. See text for a detailed description.

- 2) Four points are marked on the line joining the midpoints at an empirically selected distance of 25 pixels (so that two points lie well outside the vertebra and the other two points lie well within the vertebra) from either midpoint, as shown in Fig. 14(b).
- 3) For each diagonal pair of corner points, two points are marked on the interior side of the line joining them at an empirically selected distance of 20 pixels (so that the points lie well within the vertebra), as shown in Fig. 14(c). For each of the corner points, a point is marked at an experimentally selected distance of 15 pixels (so that the points lie well outside the vertebra) on the line perpendicular to the diagonal line [see Fig. 14(c)], and for a superior (inferior) corner point, in a direction along this perpendicular that will place the point above (below) the superior (inferior) edges. This concludes the generation of the control points for the four contours [see Fig. 14(d)].

Fig. 14(e)–(h) shows the initial positive upper, the negative upper, the negative lower, and the positive lower contours, respectively. The aforementioned procedure aims to ensure that the contours are not initialized within the upper or lower double edges. This allows for reduction in the computational workload by defining only four, rather than eight, boundaries.

5) *Specification of Forces and Snake Movement:* The internal forces are specified to be different for the positive and negative contours. For the positive upper and lower contours, the internal force is a combination of elastic, bending, and the compression pressure forces. On the other hand, for the negative upper and lower contours, the internal force is a combination of elastic, bending, and the expansion pressure forces. As mentioned earlier, the compression/expansion pressure forces are added to aid the contours in overcoming noisy pixels and reducing the influence of neighboring vertebrae. The external force used is the positive DGVF force for the positive edges and the negative DGVF force for the negative edges. Thus, the total force that drives the four contours is the aggregate of the internal and external forces given as follows:

$$\begin{aligned}
 F_x = & -\alpha \frac{d^2 x(s)}{ds^2} + \beta \frac{d^4 x(s)}{ds^4} + \rho \frac{dy(s)}{ds} \\
 & + (u^+ \times \max\{\cos(\theta), 0\} \\
 & - u^- \times \min\{\cos(\theta), 0\})|_{(x(s), y(s))} \quad (24)
 \end{aligned}$$

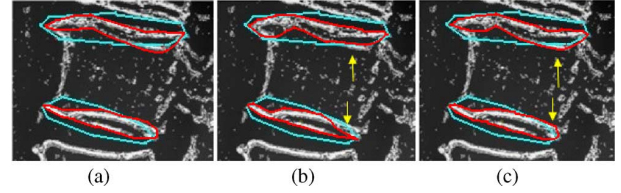


Fig. 15. Demonstration of the efficacy of DGVF forces. (a) Initialization of the four open contours shown in cyan and the ground truth is shown in red. (b) Erroneous result (shown in red) obtained using traditional GVF forces. (c) Correct result shown in red with DGVF forces.

$$\begin{aligned}
 F_y = & -\alpha \frac{d^2 y(s)}{ds^2} + \beta \frac{d^4 y(s)}{ds^4} - \rho \frac{dx(s)}{ds} \\
 & + (v^+ \times \max\{\sin(\theta), 0\} \\
 & - v^- \times \min\{\sin(\theta), 0\})|_{(x(s), y(s))} \quad (25)
 \end{aligned}$$

Here, F_x and F_y are the total forces acting on the point $(x(s), y(s))$ in the x - and y -directions, respectively. A total of four snakes were evolved by these forces to detect the double edges on each lumbar vertebra, and there are five vertebrae in each image (L1–L5). Hence, there are 20 snakes operating on each lumbar vertebrae image to detect the double edges.

While the effect of DGVF forces was presented in Fig. 8 using a synthetic image, in Fig. 15, we demonstrate the same on a real example by comparing it with gradient vector flow (GVF) snakes [22]–[25]. It is interesting to note that although the direction of the pressure force is known, traditional GVF snakes could only detect the double edges accurately if the initial contour completely enclosed the double edges. Consider Fig. 15(a) that shows the preprocessed vertebra and its initial contour in cyan. Fig. 15(b) shows the erroneous result obtained using traditional GVF snakes (segmentation error = 2.7 pixels). The arrow marks in Fig. 15(b) indicate that the initial contour does not completely enclose the double edges and because GVF snakes are unable to distinguish between an inner and an outer boundary, the snakes latch on to incorrect edges. Fig. 15(c) shows the result (red) obtained by using DGVF forces, representing a segmentation error of only 0.7 pixels. This demonstrates the importance of using DGVF forces, which effectively remove the impractical condition of requiring the initial contour to enclose the target double edges.

III. RESULTS AND DISCUSSION

This section discusses the accuracy of the proposed double-edge detection technique and its role in assessing vertebral deformities in the lumbar spine.

A. Double-Edge Detection Accuracy

As noted in the Section I, the Lister Hill National Center for Biomedical Communications, an R&D division of the U.S. National Library of Medicine, maintains a large collection of lumbar spine X-ray images. We randomly selected 100 lumbar vertebrae images from this database and processed them using the proposed algorithm. The ground truth for these 100 images was established by manually landmarking the four boundaries

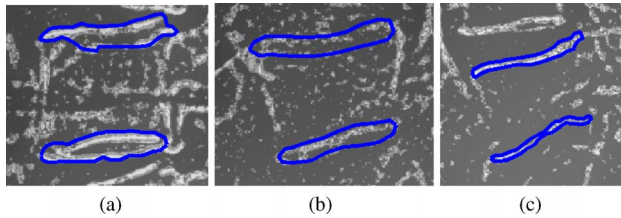


Fig. 16. Examples of manually landmarked (shown in blue) lumbar spine images that were rated by the radiologists as (a) good, (b) reasonable, and (c) not good.

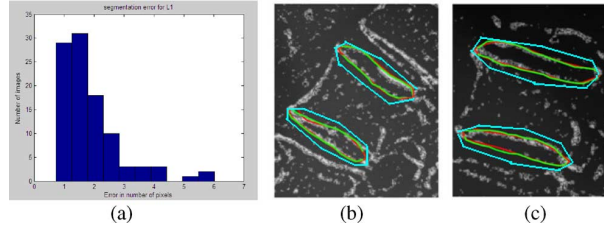


Fig. 17. (a) Double-edge detection error distribution for L1. Error is average of point-to-point differences between PODGVF solution contour and ground truth contour, for both upper and lower double edges. (b) and (c) Ground truth is manually marked in green, the double-edge detection result is shown in red and the initialization is shown in cyan. (b) Detection error = 0.7364 pixels. (c) Detection error = 0.7672 pixels.

corresponding to the double edges. Fifty percent of the landmarked boundaries were then randomly selected for review by two radiologists who graded the manual segmentations as either “good,” “reasonable,” or “not good.” The results of this review process showed that 92% of the cases were rated as “good” by the radiologists. Fig. 16(a)–(c) shows examples of each of these ratings. Four open contours were initialized to detect the double edges of each vertebra, with parameter values of $\alpha = .5$, $\beta = .01$, and $|\rho| = .02$ for each PODGVF snake. Each snake was set to evolve for a maximum of 300 iterations. The validity of the double-edge detection results was analyzed by measuring the detection error, calculated as a point-to-point distance between the detected double edges and the manually landmarked ground truth. Fig. 17(a) shows the average point-to-point detection error distribution for the four double edges corresponding to L1 of these 100 images.

Two examples with low detection errors of .7364 and .7672 pixels are shown in Fig. 17(b) and (c), respectively. In Fig. 17(c), even though the positive upper edge is broken and the positive lower edge is fragmented, the PODGVF snakes perform well with respect to detecting both edges.

Table I shows the percentage of images having an error less than 2.5 pixels. We observe that the detection error is higher for vertebra L5 than that for the other vertebrae. This happens because, for most of the images, the bottom edges of L5 are very subtle, causing them to get “washed away” during the pre-processing step. It can be observed that most of the images have a detection error less than 2.5 pixels. As an illustration, Fig. 18 shows two examples with detection errors close to 2.5 pixels. By visually comparing the double edge results to the radiologist-verified ground truth, it was deemed that a segmentation error of 2.5 pixels and lesser was acceptable. Also, the major sources

TABLE I
PERCENTAGE OF IMAGES HAVING DISTRIBUTION ERRORS LESS THAN 2.5 PIXELS

Vertebra	% of images having an error < 2.5 pixels
L1	89
L2	92
L3	87
L4	82
L5	75

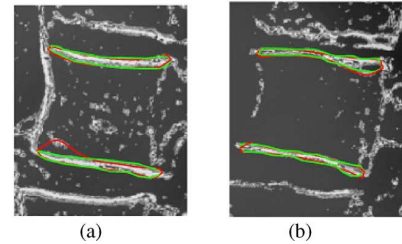


Fig. 18. Examples with detection errors close to 2.5 pixels. Ground truth is shown in green and the final result in red. (a) Detection error = 2.4773 pixels. (b) Detection error = 2.4428 pixels.

of false positives and false negatives in this study were found to be: 1) noise in the preprocessed image; 2) presence of broken edges; and 3) complete or partial absence of vertebra L5 from the radiographic images.

The previous experiment served to illustrate the accuracy of the proposed approach. Since, this is a stepwise procedure, it should be noted that the accuracy of the proposed approach hinges on the result produced by ASM. Thus, an experiment was conducted in order to address the sensitivity of the algorithm to the placement of the initial contours. Since the initial contour is determined based on the four corner points obtained from the ASM result, this experiment focuses on quantifying the double-edge segmentation errors by perturbing the four corner points of each of the five lumbar vertebrae. This involves randomly perturbing the contour points corresponding to the vertebra corners within a 10×10 square region. The size of the region was empirically determined after looking through the results of ASM in a set of 2000 images. It was observed that the 10×10 region provides for significant variability in the position of the initial contours, while ensuring that they do not cross over to the neighboring vertebrae. After the four corner points have been randomly perturbed, the initial contour is generated, the double edges are segmented, and the segmentation error is quantified using the ground truth. The aforementioned procedure was conducted, a total of ten times for each of the five lumbar vertebrae in the set of 100 images that were used for the study. Table II reports the mean and standard deviation of the segmentation errors that were obtained from this experiment. It can be seen that the average values of the segmentation error are within the acceptable range of 2.5 pixels, which serves to demonstrate the robustness of the proposed approach with respect to initial contour perturbations.

TABLE II
SENSITIVITY ANALYSIS TO CONTOUR INITIALIZATION

Vertebra	Average Segmentation error (pixels)	Standard deviation of the segmentation error (pixels)
L1	1.8	1.02
L2	1.7	.79
L3	1.7	.71
L4	1.8	.75
L5	2.3	1.06

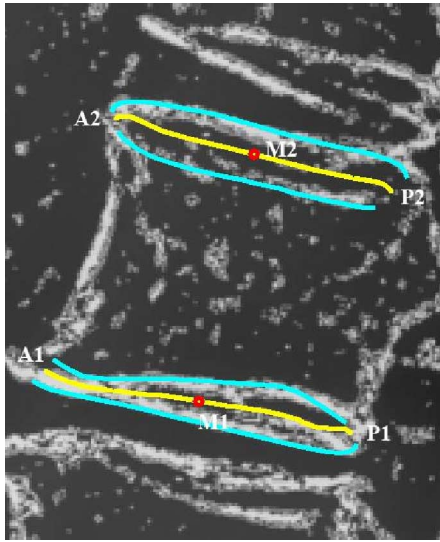


Fig. 19. Detected double edges are shown in cyan. The mean contours (yellow) are obtained by averaging the double edges. M2 and M1 (red) are the mid-points of the mean contours.

B. Vertebral Deformity Assessment

Diagnosing vertebral deformities is a critical factor in the assessment of osteoporosis. Often times, these deformities in the vertebral shape are considered by radiologists as indicators of spinal fracture. For a review of comparative quantitative methods used to assess fracture, see [7]. The vertebral deformities can be widely classified into three categories, namely biconcave deformity, crush deformity, and wedge deformity. The method employed in [5] may be used to assess the severity of these deformities. Three important measurements can be made in order to classify the lumbar vertebra as deformed or normal, namely H_a (anterior height), H_p (posterior height), and H_m (midvertebral height). These heights are usually obtained by placing six morphometric points by a radiologist on each vertebra [2]. These six points can be automatically detected by using the mean contours, which in turn, can be obtained from the double edges and the corner points of each vertebra. In Fig. 19, the detected double edges are shown in cyan. The mean contours (yellow) are obtained by averaging the double edges. In Fig. 19, note that M_2 and M_1 (red) represent the midpoints of the mean contours. A_2 and A_1 correspond to the anterior end points, whereas P_2 and P_1 are the posterior end points. These anterior and posterior end points are obtained from the four corner points detected earlier.

Within this framework, the anterior, posterior, and superior heights can be calculated using $H_a = \|A_2 - A_1\|$, $H_p = \|P_2 - P_1\|$, and $H_m = \|M_2 - M_1\|$, respectively. The Melton approach [26] may be used to differentiate the deformities by measuring the following ratios.

- 1) Biconcave deformity: H_m/H_p .
- 2) Wedge deformity: H_a/H_p .
- 3) Crushing deformity: $H_p/H_p(+1)$, $H_p/H_p(-1)$, $H_a/H_a(+1)$, and $H_a/H_a(-1)$. Here +1 and -1 stand for the upper and lower adjacent vertebra, respectively.

A threshold of .85 of the mean value of the ratios can be used to determine a deformity [26].

IV. CONCLUSION

Double-edge detection, whether it is done implicitly or explicitly, is an important factor for the assessment of injury or vertebral collapse. In addition, automatic detection of double edges enables fast and objective extraction of important morphometric measurements that could be used to develop both computer-aided diagnostic tools, as well as content-based image retrieval (CBIR) systems [27]. We took the approach of customizing DGVF snake models to detect the vertebral double edges in lumbar spine radiographs. In particular, we combined open contoured DGVF snakes with appropriately defined pressure forces to achieve accurate detection of vertebral double edges in the presence of noise and in the neighborhood of adjacent vertebrae. The efficacy of the proposed algorithm was established by its application on a set of 100 lumbar spine images, followed by a quantitative evaluation of results. The algorithm achieved a detection error of less than 2.5 pixels for 85% of the test images, when evaluated against analyst-generated and radiologist-verified ground truth.

Although the relevance of double-edge detection to vertebral morphometry was clearly illustrated in Section III-B, and while sufficient evidence exists in the literature [2], [7]–[9] to substantiate its necessity for accurate morphometric measurements, further studies are needed to quantify the anticipated level of accuracy and to assess its significance.

REFERENCES

- [1] [Online]. Available: <http://www.back.com>
- [2] H. K. Genant, C. Y. Wu, K. C. Van, and M. C. Nevitt, "Vertebral fracture assessment using a semiquantitative technique," *J. Bone Miner. Res.*, vol. 8, pp. 1137–1148, 1993.
- [3] S. Kasai, F. Li, J. Shiraishi, Q. Li, and K. Doi, "Computerized detection of vertebral compression fractures on lateral chest radiographs: Preliminary results with a tool for early detection of osteoporosis," *Med. Phys.*, vol. 33, no. 12, pp. 4664–4674, Dec. 2006.
- [4] S. Kasai, F. Li, J. Shiraishi, and K. Doi, "Usefulness of computer-aided diagnosis schemes for vertebral fractures and lung nodules on chest radiographs," *Amer. J. Roentgenol.*, vol. 191, no. 1, pp. 260–265, Jul. 2008.
- [5] S. Casciaro and L. Massotier, "Automatic vertebral morphometry assessment," in *Proc. Conf. IEEE EMBS*, Aug., 2007, pp. 23–26.
- [6] M. Cherukuri, R. J. Stanley, R. Long, S. Antani, and G. Thoma, "Anterior osteophyte discrimination in lumbar vertebrae using size-invariant features," *Comput. Med. Imag. Graph.*, vol. 28, pp. 99–108, 2004.
- [7] M. Jergas and R. San Valentin, "Techniques for the assessment of vertebral dimensions in quantitative morphometry," in *Vertebral Fracture in Osteoporosis* (Osteoporosis Research Group), H. K. Genant *et al.*, Ed. San Francisco, CA: University of California, 1995.

- [8] R. Smith-Bindman, S. R. Cumings, P. Steiger, and H. K. Genant, "A comparison of morphometric definitions of vertebral fracture," *J. Bone Miner. Res.*, vol. 6, no. 1, pp. 25–34, 1991.
- [9] J. C. Gardner, L. G. Yaffe, J. M. Johansen, G. von Ingersleben, and C. H. Chesnut, III, "Problems with six point vertebral morphometry," *Proc. SPIE Med. Imag.*, vol. 3338, no. 2, pp. 107–117, 1998.
- [10] T. C. F. Tan, D. J. Sartoris, and D. Resnick, "Differential diagnosis of osteoporotic vertebral fractures: Pathology and radiology," in *Vertebral Fracture in Osteoporosis*, H. K. Genant, M. Jergas, and C. Van Kuijk, Eds. San Francisco, CA: Radiology Research and Education Foundation, University of California, 1995, pp. 71–94.
- [11] G. Zamora-Camarena, "Automatic segmentation of vertebrae from digitized X-ray images," Ph.D. thesis, Texas Tech Univ., Lubbock, TX, 2002.
- [12] P. Smyth, C. Taylor, and J. Adams, "Vertebral shape: Automatic measurement with active shape models," *Radiology*, vol. 211, pp. 571–578, 1999.
- [13] M. Roberts, T. Cootes, and J. Adams, "Vertebral shape: Automatic measurement with dynamically sequenced active appearance models," in *Proc. 8th MICCAI Conf.*, 2005, pp. 2733–2740.
- [14] M. G. Roberts, T. F. Cootes, and J. E. Adams, "Automatic segmentation of lumbar vertebrae on digitised radiographs using linked active appearance models," *Proc. Med. Image Understanding Anal.*, vol. 2, pp. 120–124, 2006.
- [15] B. Howe, A. Gururajan, H. Sari-Sarraf, and R. Long, "Hierarchical segmentation of cervical and lumbar vertebrae using a customized hough transform and extensions to active appearance models," in *Proc. SSIAI, IEEE Comput. Soc.*, 2004, pp. 182–186.
- [16] J. Cheng and S. W. Foo, "Dynamic directional gradient vector flow for snakes," *IEEE Trans. Image Process.*, vol. 15, no. 6, pp. 1563–1571, Jun. 2006.
- [17] J. Tang, S. Millington, S. T. Acton, J. Crandall, and S. Hurwitz, "Ankle cartilage surface segmentation using DGVF snake," in *Proc. Int. Conf. Image Process.*, 2004, pp. 2745–2748.
- [18] C. Fox, *An Introduction to Calculus of Variations*. London, U.K.: Oxford Univ. Press, 1950.
- [19] M. Kass, A. Witkin, and D. Terzopoulos, "Snakes: Active contour models," *Int. J. Comput. Vis.*, vol. 1, no. 4, pp. 321–331, 1987.
- [20] L. D. Cohen, "On active contour models and balloons," *CVGIP: Image Understanding*, vol. 53, no. 2, pp. 211–218, Mar. 1991.
- [21] J. N. Otsu, "A threshold selection method from gray-level histograms," *IEEE Trans. Syst., Man, Cybern.*, vol. SMC-9, no. 1, pp. 62–66, Jan. 1979.
- [22] C. Xu and J. L. Prince, "Snakes, shapes and gradient vector flow," *IEEE Trans. Image Process.*, vol. 7, no. 3, pp. 359–369, Mar. 1998.
- [23] C. Xu and J. L. Prince, "Generalized gradient vector flow external forces for active contours," *Signal Process.*, vol. 71, pp. 131–139, 1998.
- [24] C. Xu and J. L. Prince, "Gradient vector flow: A new external force for snakes," in *Proc. IEEE Conf. Comput. Vis. Pattern Recognit.*, 1997, pp. 66–71.
- [25] C. Xu, "Deformable models with application to human cerebral cortex reconstruction from magnetic resonance images," Ph.D. thesis, Johns Hopkins Univ., Baltimore, MD, Jan. 1999.
- [26] L. J. Melton, S. H. Kan, M. A. Frye, H. W. Wahner, W. M. O'Fallon, and B. L. Riggs, "Epidemiology of vertebral fractures in women," in *Amer. J. Epidemiol.*, vol. 129, no. 5, pp. 1000–1011, May 1989.
- [27] S. Antani, J. Cheng, J. Long, R. Long, and G. Thoma, "Medical validation and CBIR of spine X-ray images over the internet," *Proc. SPIE Electron. Imag.*, vol. 6061, pp. 1–9, 2006.



Sridharan Kamalakannan received the B.E. degree in electrical and electronics engineering from Anna University, Chennai, Tamilnadu, India, in 2005, and the M.S. degree in electrical engineering from Texas Tech University, Lubbock, TX, in 2007, where he is currently working toward the Ph.D. degree in electrical engineering.

He is also engaged as a Research Assistant at the Applied Vision Laboratory, Texas Tech University. His current research interests include image processing, machine vision, and pattern recognition.

Mr. Kamalakannan is a member of the Golden Key International Honor Society.



Arunkumar Gururajan (M'08) received the B.E. degree in electronics and communication engineering (with distinction) from Bharathidasan University, Tiruchirappalli, Tamilnadu, India, in 2001, and the M.S. and Ph.D. degrees in electrical engineering from Texas Tech University, Lubbock TX, in 2003 and 2008, respectively.

He is currently engaged as a Postdoctoral Research Associate in the Department of Electrical Engineering, Texas Tech University. He is also involved at the Fiber and Biopolymer Research Institute, Texas Tech University, where he develops machine vision systems for textile-related applications. His research interests include computer vision and statistical pattern recognition.

Dr. Gururajan is a member in the Honor Society of Phi Kappa Phi.



Hamed Sari-Sarraf received the Ph.D. degree in electrical engineering from the University of Tennessee, Knoxville, TN, in 1993.

He was a Postdoctoral Research Associate in U.S. Department of Energy's Oak Ridge National Laboratory (ORNL) for one year, then he joined ORNL's Image Science and Machine Vision Group as a Research Staff Member. In 1999, he was a Faculty in the Department of Electrical and Computer Engineering, Texas Tech University, Lubbock, TX, where he is currently an Associate Professor and is the Director

of the Applied Vision Laboratory. He has authored or coauthored more than 80 scientific papers and holds eight patents. His research interests include the applications of computer vision in industrial monitoring and medical diagnosis.

Prof. Sari-Sarraf is an Associate Editor of SPIE's Journal of Electronic Imaging and a member of SPIE.



Rodney Long (M'76) received the B.A. and M.A. degrees in mathematics from the University of Texas, Austin, TX, in 1971 and 1976, respectively; and the M.A. degree in applied mathematics from the University of Maryland, College Park, MD, in 1987.

Since 1990, he is an Electronics Engineer in the Communications Engineering Branch, National Library of Medicine, Bethesda, MD. He was engaged in industry as a software developer and an engineer for IBM. He was also involved in the medical corps of the U.S. Army. He has authored or coauthored several

dozen journal and conference papers in these fields. His current research interests include telecommunications, image processing, and scientific/biomedical databases.

Mr. Long is also a longstanding member of the Mathematical Association of America.



Sameer Antani received the B.E. degree in computer from University of Pune, Maharashtra, India, in 1994, and the M.E. and Ph.D. degrees in computer science and engineering from the Pennsylvania State University, University Park, PA, in 1998 and 2001, respectively.

He is currently a Staff Scientist with the Lister Hill National Center for Biomedical Communications, National Library of Medicine, U.S. National Institutes of Health, Bethesda, MD. His research interests include multimodal information retrieval, data management in large biomedical multimedia archives, content-based indexing, and retrieval of biomedical images.

He is a member of IEEE Computer Society. He is engaged in the Steering Committee for IEEE Symposium for computer-based medical systems. He is a Reviewer for several journals including various IEEE transactions.